Journal of Alloys and Compounds 1080 (2026) 190998

Contents lists available at ScienceDirect

Journal of Alloys and Compounds

journal homepage: www.elsevier.com/locate/jalcom

From fluorite to pyrochlore: Linking structure and redox-active cations to transport properties in rare-earth oxides

P. Mowe [a], H. Glück [b], T. Jüstel [c], M. Winter [a,d], K. Neuhaus [a,*]

[a] Forschungszentrum Jülich GmbH, Institute of Energy Materials and Devices (IMD-4): Helmholtz Institute Münster (HI MS), Corrensstr. 46, Münster, DE-48149, Germany
[b] University of Münster, Institute of Inorganic and Analytical Chemistry, Corrensstr. 28/30, Münster, DE-48149, Germany
[c] FH Münster University of Applied Sciences, Department of Chemical Engineering, Stegerwaldstraße 39, Steinfurt, DE-48565, Germany
[d] University of Münster, MEET Battery Research Center, Institute of Physical Chemistry, Corrensstr. 46, Münster, DE-48149, Germany

ARTICLE INFO

Keywords:
Fluorite/Pyrochlore-Type Oxides
Mixed Ionic-Electronic Conductivity
Hebb-Wagner Polarization
Proton Conduction

ABSTRACT

Due to their unique structural and electronic properties, acceptor-doped ceria and zirconia materials with the general formula $A_2^{3+}B_2^{4+}O_7$ are promising candidates for electronic and energy applications. Using $La_2Ce_2O_7$ as a benchmark, this study investigates the relationship between structural motifs and electronic behavior of cerates and zirconates containing Pr as an (additional) redox-active species. Structural analysis was performed using X-ray diffraction and Raman spectroscopy revealing disordered fluorites for $Pr_2Ce_2O_7$ and $La_2Ce_2O_7$ with an increasingly ordered structure for $LaPrCeZrO_7$ and $Pr_2Zr_2O_7$ having a pyrochlore structure. Using a micro-contact Hebb-Wagner method alongside electrochemical impedance spectroscopy (EIS) in various atmospheres provided precise information about the partial electronic, proton, and oxygen ion conductivities. The results reveal clear correlations between structural features and transport properties with materials containing Ce and Pr showing markedly increased electrical conductivity. $Pr_2Zr_2O_7$ exhibits the highest proton transference number among comparable materials below 500 °C, underlining its potential for low- to intermediate-temperature proton-conducting applications.

1. Introduction

Acceptor-doped ceria and zirconia have attracted attention due to their versatile structural characteristics and tunable electronic and ionic properties, making them promising candidates for a wide range of applications, including energy conversion, sensors, and electronic devices. [1–6] With ongoing advancements in materials science, these materials are playing an increasingly important role in developing next-generation systems for sustainable energy storage and conversion. Previous studies have shown that doped cerates and zirconates-based ceramics have high ionic conductivity at temperatures above 800 °C, which could open the door for application of ion conductors with the general formula $A_2^{3+}B_2^{4+}O_7$. [7–9]

In recent years, research has focused on $La_2Ce_2O_7$ electrolytes that exhibit both proton and oxide-ion conductivity, particularly with regard to their use in fuel cells, electrolyzer cells, and ammonia synthesis. [9–11] Their complex structures allow for the incorporation of redox-active elements, which can strongly influence both electronic and ion transport. [12] Attention has expanded to include praseodymium-containing analogues, in which lanthanum is partially or fully replaced by praseodymium. These compounds, such as $Pr_2Ce_2O_7$ and $Pr_2Zr_2O_7$, crystallize in fluorite- or pyrochlore-type structures. [13]

Of the various dopants investigated, praseodymium is noteworthy as it can exist in Pr^{3+} and Pr^{4+} oxidation states within Ce–Zr solid solutions, even under oxidizing conditions at high temperatures. This mixed-valence state improves important properties such as material reducibility, mobile oxygen vacancy concentration, and oxygen storage capacity, all of which are essential for optimal electrochemical performance. [14–16]

Furthermore, the proportion of Pr^{3+} ions increases as the zirconium content rises. This behavior is caused by differences in ionic radii and bond lengths. The shorter Zr^{4+}–O^{2-} bonds can accommodate and stabilize the larger Pr^{3+}–O^{2-} bonds within the crystal lattice. Consequently, the incorporation of Zr^{4+} promotes a more flexible oxygen sublattice, thereby enhancing defect formation and redox activity. These structural adjustments influence the distribution of praseodymium (Pr) oxidation

* Corresponding author.
E-mail address: k.neuhaus@fz-juelich.de (K. Neuhaus).

https://doi.org/10.1016/j.jallcom.2026.190998
Received 21 July 2026; Received in revised form 26 August 2026; Accepted 6 September 2026
Available online 11 September 2026

states and affect the concentration and mobility of oxygen vacancies. Both are critical for ionic conductivity and overall electrochemical performance. Therefore, adjusting the Pr/Zr ratio is a practical method for optimizing the structural and transport properties of these mixed oxides. [17–19]

Although Pr-based materials exhibit promising electrochemical properties, the pyrochlore family is comparatively understudied, especially with regard to the structure-property relationships that govern ionic transport. [20,21]

The present work examines Pr-containing fluorite- and pyrochlore-type compounds to advance our fundamental understanding of these materials and their technological potential. However, the relationship between specific structural motifs and resulting electronic, protonic, and oxide-ion transport mechanisms remains unclear. Additionally, systematic electrochemical impedance spectroscopy (EIS) studies on these materials are scarce, leaving key aspects of their ionic transport behavior unresolved.

In this study, the interplay between structural motifs and transport properties in fluoride and pyrochlore structures is investigated. X-ray diffraction and Raman spectroscopy for structural characterization are combined with work function and band gap measurements, as well as partial electrical conductivity and electrochemical impedance spectroscopy (EIS) to disentangle the contributions of electronic, protonic, and oxygen ion conductivity. Understanding these correlations allows not only a more complete picture of the fundamental conduction mechanisms in pyrochlores but also provides guidance for tailoring their properties through targeted compositional and structural modifications. Ultimately, this approach seeks to bridge the gap between microscopic structural features and macroscopic transport behavior, offering strategies for the rational design of functional materials for next-generation energy and electronic applications.

2. Materials and methods/ experimental

2.1. Sample preparation

The synthesis of $Pr_2Ce_2O_7$, $La_2Ce_2O_7$, $LaPrCeZrO_7$, and $Pr_2Zr_2O_7$ was accomplished through the Pechini process. [22] The initial materials required for the synthesis are listed in Table 1 of the Supporting Information (S.I.). The metal nitrates required for the sol-gel process were diluted in deionized water within a flask, followed by thorough stirring until complete dissolution was achieved. Citric acid monohydrate ($n_{\text{citric acid monohydrate}} = 2 \bullet n_{\text{cations}}$) was added under stirring and heating to 50 °C as a chelating agent for complexation. Following a one-hour waiting period, propane-1,3-diol ($n_{\text{diol}} = 4 \bullet n_{\text{cations}}$) was added for the polycondensation process. After 30 min stirring at 80 °C, the solution was gelled at 140 °C for 1 h, afterwards at 100 °C for 16 h and followed by calcination at 400 °C for 2 h and 600 °C for 1 h with a heating/cooling rate of 5 K min^{-1}. The calcinated compounds were ground in a mortar and then pressed into 8-mm-diameter pellets at 20 kN for 3 min. The pellets were sintered at 1400 °C for 10 h with a heating/cooling rate of 5 K min^{-1}. All samples had a density exceeding 95%.

2.2. XRD

For powder X-ray diffraction (XRD) analysis, the pellets were first ground in an agate mortar. Diffraction patterns were recorded on a D8 Advance diffractometer (Bruker Corporation, USA) using nickel-filtered Cu K_α radiation over a 2Θ range of 10–90°. Measurements were performed in Bragg–Brentano geometry with a one-dimensional LynxEye position-sensitive detector operated in continuous scanning mode.

2.3. Raman spectroscopy

Raman measurements were acquired with a Horiba Scientific confocal Raman microscope (LabRAM HR evolution, air-cooled CCD detector). Prior to the measurement, the system was calibrated using the silicon Raman band at 520.7 cm^{-1}. The pellets were excited by a green laser with a wavelength of 532 nm. The output power of the green laser at the sample was 34.0 mW, which was adjusted by a 25% filter to 8.5 mW. The beam was focused using a 50 × long-working distance objective (Carl Zeiss Microscopy, 9.2 mm, numerical aperture 0.5). Raman spectra were collected over seven integrations, each with a duration of 20 s. LabSpec6.7.1.1 (Horiba Scientific) was utilized to manage the microscope, collect the spectra, and evaluate the data.

2.4. Kelvin probe force microscopy

Kelvin Probe Force Microscopy (KPFM) measurements were performed under ambient conditions at room temperature using a Cypher ES (Asylum Research/Oxford Instruments, UK). Conductive Pt/Ir-coated cantilevers (PPP-NCSTPt, Nanosensors, Switzerland) were employed for the measurements. Surface topography and Volta potential maps were recorded simultaneously. The pellet samples were analyzed without any additional surface modifications. Image processing was performed using Mountains SPIP Starter 8.0 software (DigitalSurf, France).

2.5. Impedance spectroscopy

Electrical impedance spectroscopy (EIS) measurements were conducted under ambient air conditions using an AutoLab IMP potentiostat with the NOVA 2.1.6 software (Deutsche Metrohm GmbH & Co. KG) in an ROK 70/250/12 oven (ThermoConcept GmbH, Germany).

Impedance spectra under dry and humid argon atmosphere were measured using an Alpha-A frequency analyzer (Novocontrol Technologies, Germany), POT/GAL 15 V 10 A interface (Novocontrol Technologies, Germany), and a custom-made sample cell by Huber Scientific, Austria. To dry the argon (99.996 vol%, Westfalen) it was passed over silica gel (orange) and molecular sieve (3 Å). To humidify the argon it was first passed through deionized water and afterwards through a saturated solution of $Ca(NO_3)_2 \bullet 4H_2O$ at room temperature. This yielded a relative humidity of ~52% and is described as humid Ar. To establish a consistent atmosphere, the sample cell was purged with the respective gas(-mixture) for 1 h prior to starting measurement with a flow rate of 25–30 mL/min. The same flow rate was maintained throughout the measurement. The impedance spectra were measured from 200 °C to 850 °C. Each temperature was equilibrated for at least 1 h before the impedance spectra were measured. The frequency range was 1 MHz to 50 MHz and an excitation amplitude 0.04 V was used. Prior to the measurement, the samples were subjected to a polishing and sputtering process with a thin Au layer using a Quorum150T ES plus (Quorum Technologies Limited Company, UK) in order to ensure optimal electrode sample contact. The data were analyzed with the software Relaxis 3.0.23.

2.6. Hebb-Wagner type measurement

Microcontact (Hebb–Wagner-type) measurements were performed to determine the electronic partial conductivity of the samples under ambient air using an AutoLab IMP potentiostat controlled by NOVA 2.1.6 software (Metrohm GmbH & Co. KG, Germany) in an ROK 70/250/12 oven (ThermoConcept GmbH, Germany). The pellets were contacted on one side with a platinum sheet and additional fixed with platinum paste (fuelcellmaterials, USA) as counter electrode, and on the other side with a platinum microcontact as working electrode. The microcontact was encapsuled with a glass paste IP211 (Heraeus Deutschland GmbH & Co.KG, Germany) and subsequently annealed at 950 °C for 15 min. Measurements were taken from 850 °C to 300 °C with a two-hour equilibration period prior to applying voltage. The voltage was in the range of −0.03 V to −0.6 V in 0.03 V steps. For each data point the voltage was held for 20 min and the mean value of the last

5 min, the steady state current, were taken.

All electronic conductivity values were corrected for microcontact diameter. This was determined by measuring the contact imprint on the glass encapsulation using light microscopy (RNDlab, Switzerland) after the Hebb-Wagner experiment ended.

2.7. Reflection spectroscopy

An Edinburgh Instruments FS920 spectrometer equipped with a Teflon-coated integrating sphere was used to record the reflection spectra. A Xe900 arc lamp from Edinburgh Instruments, equipped with a 450 W rating and a R928 detector (Hamamatsu, Japan), was utilized for the measurement. The detector was operated at a temperature of −20 °C using a Peltier cooling system. The electromagnetic waves are directed through the spectrometer by means of a lens optic. Initial measurements were obtained in the wavelength range from 250 nm to 500 nm, with a step size of 1.0 nm, and subsequently from 480 nm to 800 nm, employing a 455 nm filter and a step size of 1.0 nm. The measurement procedure was replicated three times. Both spectra were combined at 490 nm. Barium sulfate (BaSO4; 99.99%; Sigma-Aldrich) was utilized as a white reflection standard.

3. Results and discussion

Structural characterization was done by XRD and Raman measurements as can be seen in Fig. 1. All lattice parameters are listed in Table 2 in the S.I. The XRD pattern of $Pr_2Ce_2O_7$ reveals a clear, single-phase fluorite ($Fm\bar{3}m$) structure with a lattice parameter of 5.441 Å. Among all the compounds, $La_2Ce_2O_7$ exhibits the largest lattice parameter (5.612 Å) due to the large radius of La. $La_2Ce_2O_7$ exhibits reflections that are indicative of the fluorite structure. The present literature has discussed contrary observations regarding whether $La_2Ce_2O_7$ is a fluorite or a pyrochlore [23–27] and has been described as defective fluorite with local pyrochlore attributes as we previously showed in ref. [28]. The Raman measurements show that the fluorite structure of $Pr_2Ce_2O_7$ is more ordered than that of $La_2Ce_2O_7$. However, the intensity of the 590 cm^{-1} band increases due to greater lattice desertion as the number of oxygen vacancies rises. With $LaPrCeZrO_7$ the amount and intensity of pyrochlore reflections increase compared to $La_2Ce_2O_7$, but still shows an overall fluorite structure. $Pr_2Zr_2O_7$ is a clear pyrochlore ($Fd\bar{3}m$) as can be observed by XRD and Raman measurements in Fig. 1. [29,30] In the Raman spectrum of $Pr_2Zr_2O_7$ four bands are visible which are considered as the pyrochlore fingerprints. There are two F_{2g} bands at around 380 cm^{-1} and 505 cm^{-1} and the E_g and F_{2g} mode at around 295 cm^{-1} relate to the typical O-Zr-O bending vibrations. The A_{1g} mode at around 580 cm^{-1} is assigned to the ZrO_6 bending vibrations. [31,32]

As the structure of the fluorite is approached, the two F_{2g} bands merge into a single band, and the primary band, situated at approximately 300 cm^{-1}, disappears. Concurrently, a band associated with oxygen vacancies emerges. The $LaPrCeZrO_7$ Raman spectrum displays a broad band, suggesting the presence of disorder in the lattice and a mixture of both fluorite and pyrochlore, as previously indicated by the XRD analysis. $La_2Ce_2O_7$ exhibits the characterist F_{2g} band at approximately 450 cm^{-1} for cubic cerates. This band shift is typical of heavily doped ceria, shifting 15 cm^{-1} from the 465 cm^{-1} band of undoped ceria towards lower frequencies and becoming asymmetric. [33,34] Additionally, a band at around 590 cm^{-1} is observed, which is attributable to the incorporation of La^{3+} into the lattice. This process leads to the formation of oxygen vacancies (O1), a consequence of charge equalization that occurs during doping with elements possessing a lower charge. [26,35] The band at 260 cm^{-1} corresponds to the formation of an additional oxygen vacancy, while the band at 350 cm^{-1} is regarded as a phase of the

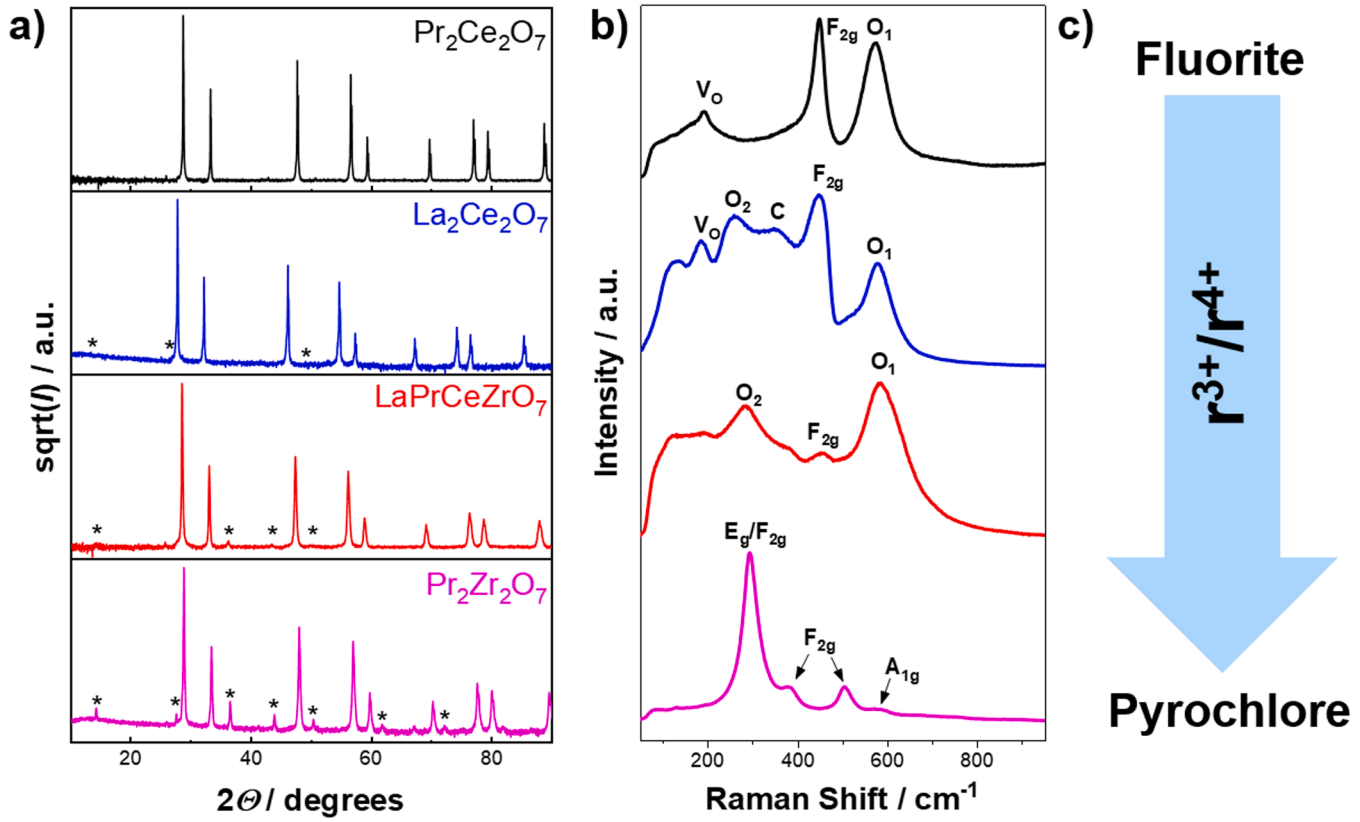

Fig. 1. a) XRD powder diffraction pattern of $Pr_2Ce_2O_7$, $La_2Ce_2O_7$, $LaPrCeZrO_7$ and $Pr_2Zr_2O_7$. * marks the pyrochlore reflections, which a clearly visible in $Pr_2Zr_2O_7$ and partly in $LaPrCeZrO_7$ and $La_2Ce_2O_7$. b) Raman spectra of $Pr_2Ce_2O_7$, $La_2Ce_2O_7$, $LaPrCeZrO_7$ and $Pr_2Zr_2O_7$ with their respective band description. c) The schematic arrow indicates the pathway from fluorite to pyrochlore, contingent upon the cation radii ratio, as supported by the XRD and Raman results.

C-type structure. The bands below 200 cm^{-1} result from vibrations associated with tetrahedral metal complexes that contain oxygen vacancies (V_O). [26,36,37]

The results of the structural characterization provide the foundation for further analysis. In the following, the electronic properties are analyzed in relation to the identified structural features, with particular emphasis on the elements exhibiting redox activity, to provide a more comprehensive understanding of the material.

The work functions of all compounds were determined from KPFM measurements of the Volta surface potential (contact potential difference) relative to the conductive AFM tip. As the work function is defined as the energy difference between the vacuum level and the Fermi level, it provides information on the position of the Fermi level, and, therefore about the electronic structure and energy level of the material. [38] A schematic energy level diagram illustrating the KPFM measurement principle is shown in Fig. 2d). All KPFM measurements were conducted under ambient air conditions. In such conditions, the surface adsorption of water and oxygen has the capacity to modify the local work function. Consequently, the reported contact potential differences (CPD) represent the equilibrium state between the ceramic surface and the surrounding atmosphere. [39,40] The mean potential from over 50 grains of three distinct pellets was calculated to determine the work function. $La_2Ce_2O_7$ exhibits the highest work function, with a value of 5.88 ± 0.09 eV. This is followed by $Pr_2Ce_2O_7$, with a value of 5.55 ± 0.06 eV, and $LaPrCeZrO_7$, with a value of 5.40 ± 0.02 eV. $Pr_2Zr_2O_7$ exhibits the lowest work function, with a value of 5.18 ± 0.03 eV (Fig. 2a).

The optical band gap was determined from the reflection spectra upon using a Tauc analysis assuming a directly allowed transition. In highly doped ceramics, the high charge carrier concentration can shift the Fermi level, slightly modifying the band structure in a phenomenon known as the Burstein–Moss shift. [41] Nevertheless, the fundamental band geometry remains that direct transitions are permitted. Therefore, electrons can move from the valence band to the conduction band without altering their crystal momentum. This results in the characteristic absorption features of direct transitions. [42–44] $Pr_2Ce_2O_7$ exhibits an optical band gap of (2.00 ± 0.05) eV, which is the lowest value reported for this class of compounds. This comparatively narrow band gap can be attributed to the presence of multiple redox-active elements (Pr^{3+}/Pr^{4+} and Ce^{3+}/Ce^{4+}), which introduce additional electronic states and enhance orbital hybridization, thereby reducing the energy separation between the valence and conduction bands. The present finding is supported by extant literature but with a different synthesis method for the compound. [42,45] $La_2Ce_2O_7$ demonstrates a band gap of 3.18 ± 0.04 eV, which is considerably smaller than that of pure CeO_2 and analogous to the value reported by Khademinia et al. who also employed a distinct synthesis method and obtained a value of 3.1 eV. [46,47] $LaPrCeZrO_7$ shows a value of 2.56 ± 0.15 eV while $Pr_2Zr_2O_7$ exhibits a band gap of 4.20 ± 0.08 eV, which is notably large. Xu et al. calculated the band structure under PBE + SOC for $Pr_2Zr_2O_7$ with an insulating band gap of 3.66 eV. [48] Here has to be noted that the optical band gap is ~200–400 meV higher than electronic band gap energy as it includes the exciton binding energy. [49]

The presence of structural disorder and point defects, such as oxygen vacancies, can also result in the introduction of additional electronic states within the band gap which then leads to the broadening and lessening of the absorption edge. [50] Consequently, the presence of a shallow absorption edge is sign of defects, disorder, or intermediate electronic states, reflecting a lower degree of structural perfection. Fifere et al. showed that UV-Vis diffuse reflectance measurements, combined with Urbach energy analysis—which quantifies the degree of

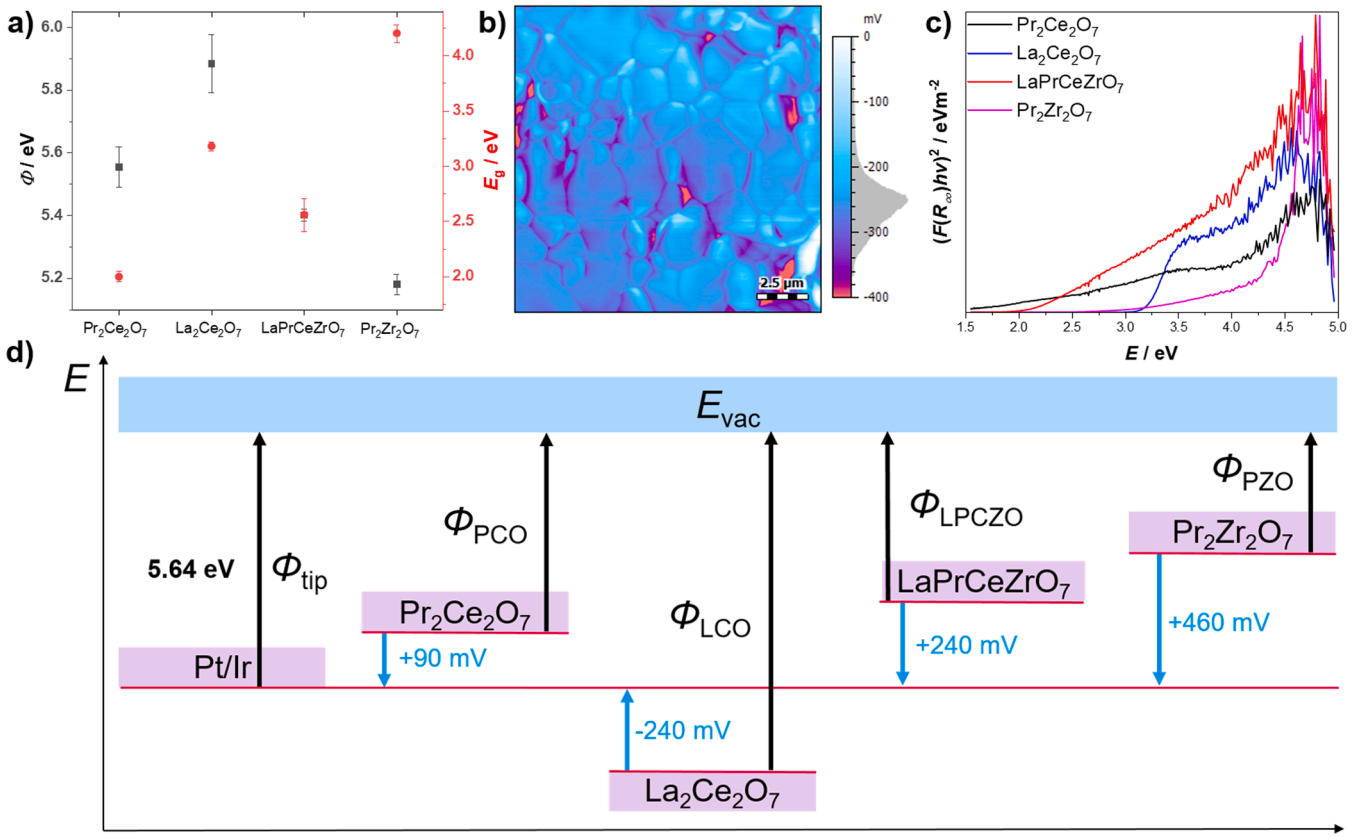

Fig. 2. a) Work function (Φ) data of $Pr_2Ce_2O_7$, $La_2Ce_2O_7$, $LaPrCeZrO_7$ and $Pr_2Zr_2O_7$ from KPFM measurements (black squares) and optical band gap energies (E_g) from the Tauc plot (red circles). b) Exemplary KPFM image of $La_2Ce_2O_7$ with grain boundaries showing lower surface potential than the bulk. c) Tauc plot for all compounds. d) Schematic energy level diagram illustrating the work functions (black) and Fermi level (red) alignment of the conductive AFM tip and the sample, as well as the resulting Volta surface potential (blue) measured by KPFM.

sub-bandgap absorption due to defects—can reveal the presence of oxygen vacancies and structural disorder in CeO_2 nanoparticles, with higher Ce^{3+} content correlating with increased disorder. [51] Moreover, as shown in Fig. 2c), $La_2Ce_2O_7$ exhibits a steeper absorption edge and a more pronounced linear region in the Tauc plot. This is in line with a lower Urbach energy and reduced electronic disorder. In contrast, $Pr_2Ce_2O_7$ shows a flatter Tauc slope, which shows enhanced sub-band gap tail states. These states arise from an increased concentration of oxygen vacancies and mixed-valence cations. Raman analysis further supports this trend by revealing more asymmetric vibrational modes for $Pr_2Ce_2O_7$, reflecting the material's higher degree of oxygen vacancies (O1).

The room-temperature band gap values provide information on the intrinsic electronic structure of the materials, while the Hebb–Wagner measurements provide access to the defect-mediated electronic transport properties under elevated-temperature conditions, thereby complementing the electronic structure analysis. [52,53] The following data show the average electronic conductivity of all compounds as a function of oxygen partial pressure.

In Fig. 3a), the oxygen partial pressure dependence of the electronic partial conductivity for $Pr_2Ce_2O_7$ is illustrated. A pronounced pO_2 dependence is observed, particularly at temperatures above 650 °C, indicating a strong contribution of redox-active charge carriers under these conditions. The presence of Pr as a second redox-active cation in $Pr_2Ce_2O_7$ results in the highest electronic partial conductivity observed among the compounds investigated at 800 °C. Below 650 °C the electronic partial conductivity decreases many orders of magnitude which can be explained as the thermally activated small-polaron hopping mechanism is no longer efficient. This phenomenon can result in comparatively low electronic conductivity at lower temperatures, despite the smaller band gap and work function of $Pr_2Ce_2O_7$. Pr and Ce provide redox-active centers, but this does not directly imply efficient electronic conductivity. Cheng et al. discussed the electronic configurations associated with Pr/Ce in [54] where Pr doped ceria (below 10 at %) forms discrete acceptor levels (Pr 4f). [55] However, considerable electronic conductivity cannot be generated by these states as the Pr 4f states are closer to the O2p valence edge than the Ce 4f conduction band. The corresponding electronic states remain localized, unless sufficient thermal activation leads to excited O2p states and their localization into the Pr 4f states. [54,56] The effect is amplified when 50% Pr-doped ceria is used. While the electronic transport decreases upon cooling, the ionic transport can be less affected due a stable vacancy network. In addition, a structural phase transition may also contribute this effect by changing the local cation environment. $La_2Ce_2O_7$ (Fig. 3b) demonstrates a qualitatively analogous response, showing a continuous dependence on oxygen partial pressure across the entire range of temperatures investigated. In contrast to $Pr_2Ce_2O_7$, no abrupt change between individual temperature steps is observed, suggesting a more gradual

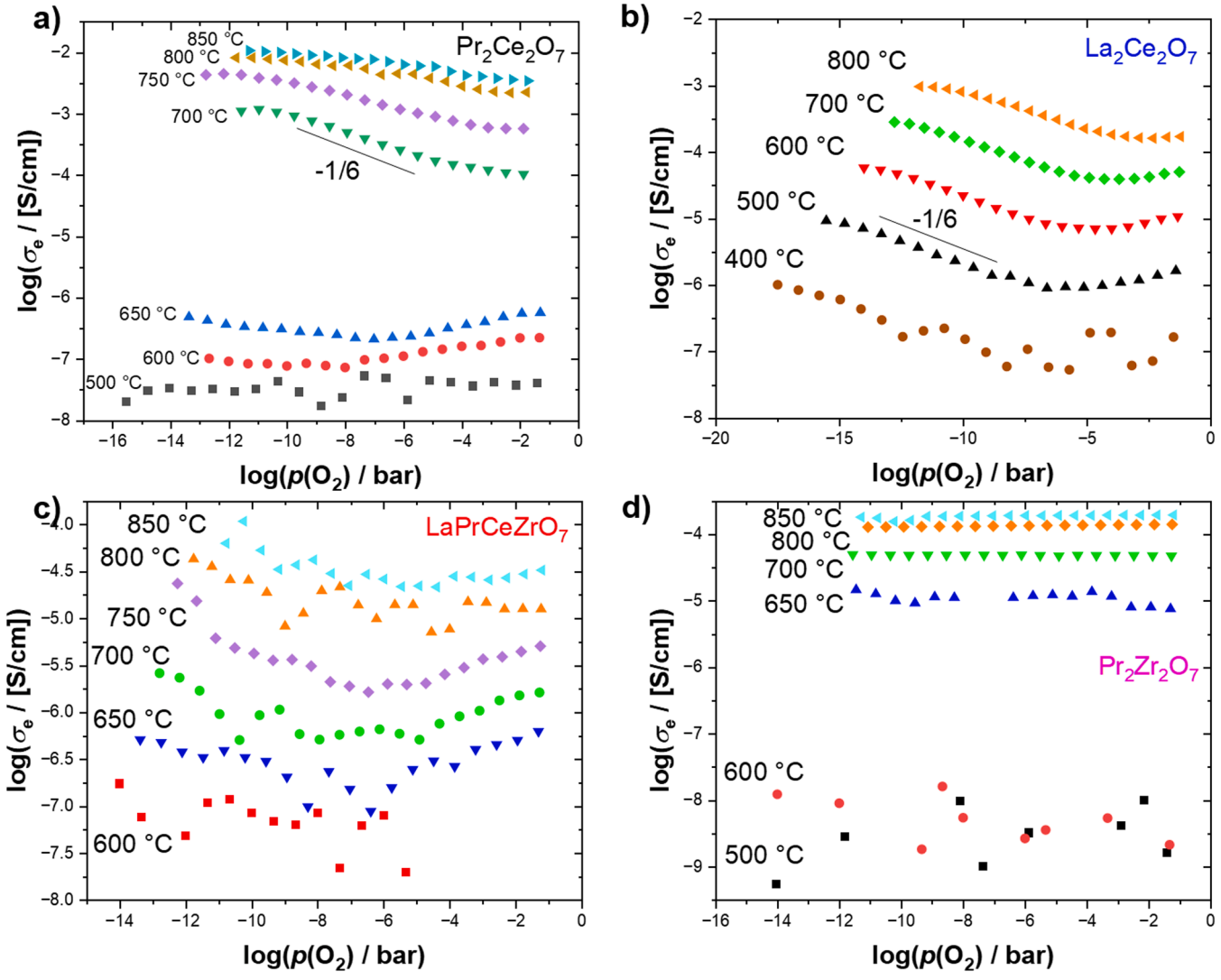

Fig. 3. Average electronic conductivity of the respective samples as a function of oxygen partial pressure and temperature.

evolution of the dominant charge carriers with temperature and oxygen chemical potential. A Raman study at various temperatures in ref. [57] revealed that $La_2Ce_2O_7$ does not undergo a phase transition within this temperature range, and that the subcrystalline phase structure remains unchanged which explains why there is no large gap in the curve between these temperatures.

In ceria-based fluorites, the pO_2 dependence of ionic conductivity is often interpreted using idealized Brouwer diagrams. At sufficiently low oxygen partial pressures, when intrinsic reduction dominates, the vacancy concentration is expected to depend on pO_2. Between the extrinsic plateau and the intrinsic reduction regime, the idealized Brouwer diagram (Fig. 4a) with 1% acceptor-doped cerium oxide predicts a transition region in which competing charge compensation mechanisms result in a pO_2 dependence with a slope of $-1/4$.

However, experimental data showed a $-1/6$ slope in ceria-based materials (Fig. 3a,b), including Pr-doped ceria and heavily A-site-substituted defect-fluorite systems, such as $La_2Ce_2O_7$. This slope is often observed at relatively high pO_2 values, and in some cases, even close to air saturation, as seen by $Pr_2Ce_2O_7$. [14]

To support the interpretation of the experimental data, we simulated Brouwer diagrams based on assumptions for a cerium oxide system with a fluorite structure and different amounts of trivalent, redox inactive acceptor dopant (full documentation in ref. [58]), enabling a direct comparison with $La_2Ce_2O_7$. Acceptor doping of cerium oxide has a pronounced impact on both the slopes of the different contributions to the total conductivity and the oxygen partial pressure range showing a stable ionic conductivity, as illustrated in Fig. 4b). Comparing the simulated Brouwer diagram with the Hebb–Wagner measurements of $La_2Ce_2O_7$ at 800 °C (Fig. 3b) reveals that the minimum of the measured partial electronic conductivity ($pO_2 \approx -3$ bar) aligns well with the simulated intersection of n-type to p-type conduction in Fig. 4b) (black and red line).

The key to understanding lies in distinguishing between the total defect population and the transport-relevant defect population. Brouwer diagrams describe thermodynamic equilibrium concentrations of all defects, while the measured conductivity depends predominantly on mobile oxygen vacancies. In addition to acceptor doping, the creation of vacancies can also be achieved through the use of redox-active elements within the compound.

Under conditions of decreasing oxygen partial pressure, the process of reduction from the small fraction of Ce^{4+} to Ce^{3+} occurs, with the escape of oxygen from the structure in order to maintain electroneutrality [59]:

$$2\ Ce_{Ce}^{x} + O_O^x \leftrightarrow 2\ Ce_{Ce}^{'} + V_O^{\bullet\bullet} + \frac{1}{2}\ O_2 \quad (1)$$

By using Pr as an additional redox-active doping agent and with small amounts of Pr^{4+}, the same reaction takes place [14]:

$$2\ Pr_{Ce}^{x} + O_O^x \leftrightarrow 2\ Pr_{Ce}^{'} + V_O^{\bullet\bullet} + \frac{1}{2}\ O_2 \quad (2)$$

These newly formed vacancies dominate ionic transport, even at relatively low concentrations. Under these conditions the oxygen vacancy concentration is described as fixed:

$$[Pr_{Ce}^{'}] \approx 2\ [V_O^{\bullet\bullet}] \quad (3)$$

which leads to the power law dependence of the oxygen vacancy concentration on pO_2 with a $-1/6$ slope [60]:

$$[V_O^{\bullet\bullet}] = \frac{1}{2}[e'] \propto P_{O_2}^{-1/6} \quad (4)$$

For $Pr_2Ce_2O_7$ and $La_2Ce_2O_7$, this behavior shows that the reduction of Ce^{4+} to Ce^{3+} creates additional oxygen vacancies relevant for transport. In $Pr_2Ce_2O_7$, the shift of the minimum of the electronic conductivity (transition from n-type to p-type conductivity) is visible at even higher pO_2 values compared to $La_2Ce_2O_7$ due to the additional redox activity of Pr. Redox-active dopants on the A-side shift the reduction to higher pO_2 values and make the $-1/6$ behavior accessible even in a more oxidizing atmospheres, but do not change the fundamental slope itself. The $-1/4$ range would be expected for both cases in an idealized Brouwer diagram, but is strongly compressed or not accessible experimentally, since the transport-dominant vacancies are formed early on by reduction. This phenomenon can be attributed to the comparatively low stability of the Ce–O bond [61,62], which results in a close coupling between reduction and oxygen vacancy formation. The observed $-1/6$ slope shows then the intrinsic reduction chemistry of the ceria host lattice, and is independent of the specific acceptor species under heavy acceptor doping conditions, where many oxygen vacancies are already present, which points out that the $-1/4$ slope is a signature of transport-active extrinsic vacancies, whereas the $-1/6$ slope reflects intrinsic, reduction-driven vacancy transport.

In $LaPrCeZrO_7$, the presence of multiple conductivity minima between 800 °C and 600 °C suggests the occurrence of competing transport mechanisms or alterations in the predominant defect species. At temperatures below 500 °C, the electronic partial conductivity falls below the limit of quantification. The comparatively low electronic conductivity of $LaPrCeZrO_7$ may be related to its structural characteristics, as the composition is located close to the pyrochlore–fluorite stability boundary. Local structural disorder or short-range ordering effects arising from this structural proximity may impede effective charge transport and contribute to the suppressed conductivity. [63]

$Pr_2Zr_2O_7$ exhibits nearly oxygen partial pressure–independent conductivity, which is in line with prior reports concerning zirconate-based compounds. [64,65] This behavior reflects a comparatively stable defect chemistry, with negligible changes in the electronic carrier

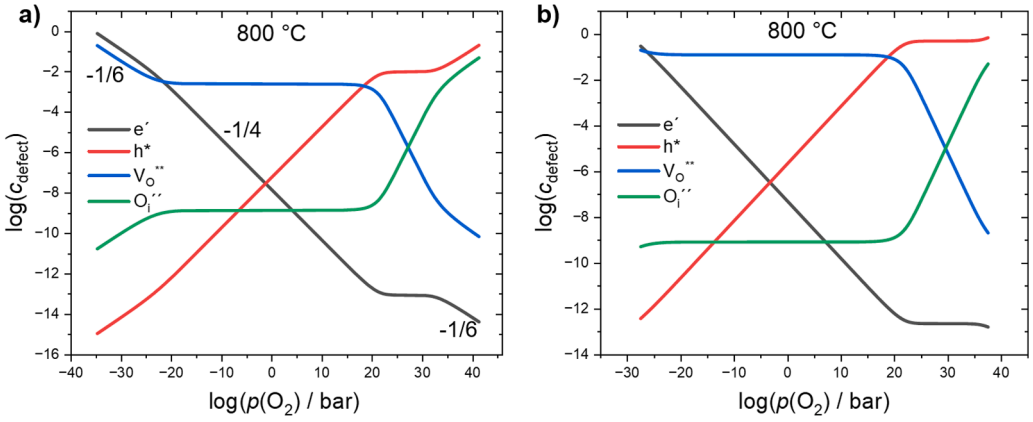

Fig. 4. a) Brouwer diagrams simulated with [58] of a) 1% acceptor-doped cerium oxide and b) 50% acceptor-doped cerium oxide at 800 °C.

concentration over the investigated pO_2 range. Although Pr is redox active and has an influence on ceria-based compounds, for $Pr_2Zr_2O_7$, the reduction of Pr is strongly suppressed energetically due to the high stability of the Zr–O bond and the isolation of Pr. [66,67] Therefore, changes in pO_2 only lead to local valence changes in cations without pronounced formation of additional oxygen vacancies which results in the fixed concentration of transport-relevant vacancies by structure and doping and remains independent of pO_2. [68]

However, a fixed oxygen vacancy concentration does not imply low ionic conductivity, but rather stable transport properties independent of oxygen partial pressure. Zirconate-based materials can show high and stable conductivities for oxygen ions and protons over a broad oxygen partial pressure range due to structurally determined vacancy concentration and sufficient defect mobility (see also Fig. 4). [69] EIS measurements of total conductivity allow a direct comparison of the transport performance of ceria- and zirconate-based systems, showing that high conductivities can result from both redox-driven and structurally fixed defect chemistry.

In addition to the electronic conductivity, the total conductivities of all compounds are investigated with impedance spectroscopy under three different atmospheres: (a) air, (b) Ar + 50% humidity, and (c) Ar. In Fig. 5 each compound is shown with all respective conductivity measurements in one graph. Among the analyzed materials, $Pr_2Ce_2O_7$ exhibits the highest total conductivity in all atmospheres. It should be noted that a positive imaginary part was observed in the impedance spectra of $Pr_2Ce_2O_7$ up to 500 °C, indicative of inductive behavior which can be explained by redox kinetics of mobile point defects, rather than experimental artifacts (see also SI Figure 9). [70] $Pr_2Zr_2O_7$ does not show this behavior since the presence of Zr effectively isolates the Pr^{3+} ions and thus suppresses the redox activity within the lattice. This limits the extent of coupled redox processes between A and B cations, thereby reducing the chemical inductance. [48]

$La_2Ce_2O_7$ shows high total conductivity at 800 °C in all atmospheres but decreases more rapidly with decreasing temperature compared to the other compounds. $LaPrCeZrO_7$ maintains relatively high total conductivities across the measured temperature range, indicating effective electronic and ionic transport in this mixed composition. $Pr_2Zr_2O_7$ maintains relatively high total conductivity at elevated temperatures under Ar due to thermal activation, but decreases below 500 °C, in contrast to measurements under air or humid atmospheres, where the conductivity remains markedly higher. This conductivity drop, which was also observable in the partial electronic conductivity measurements

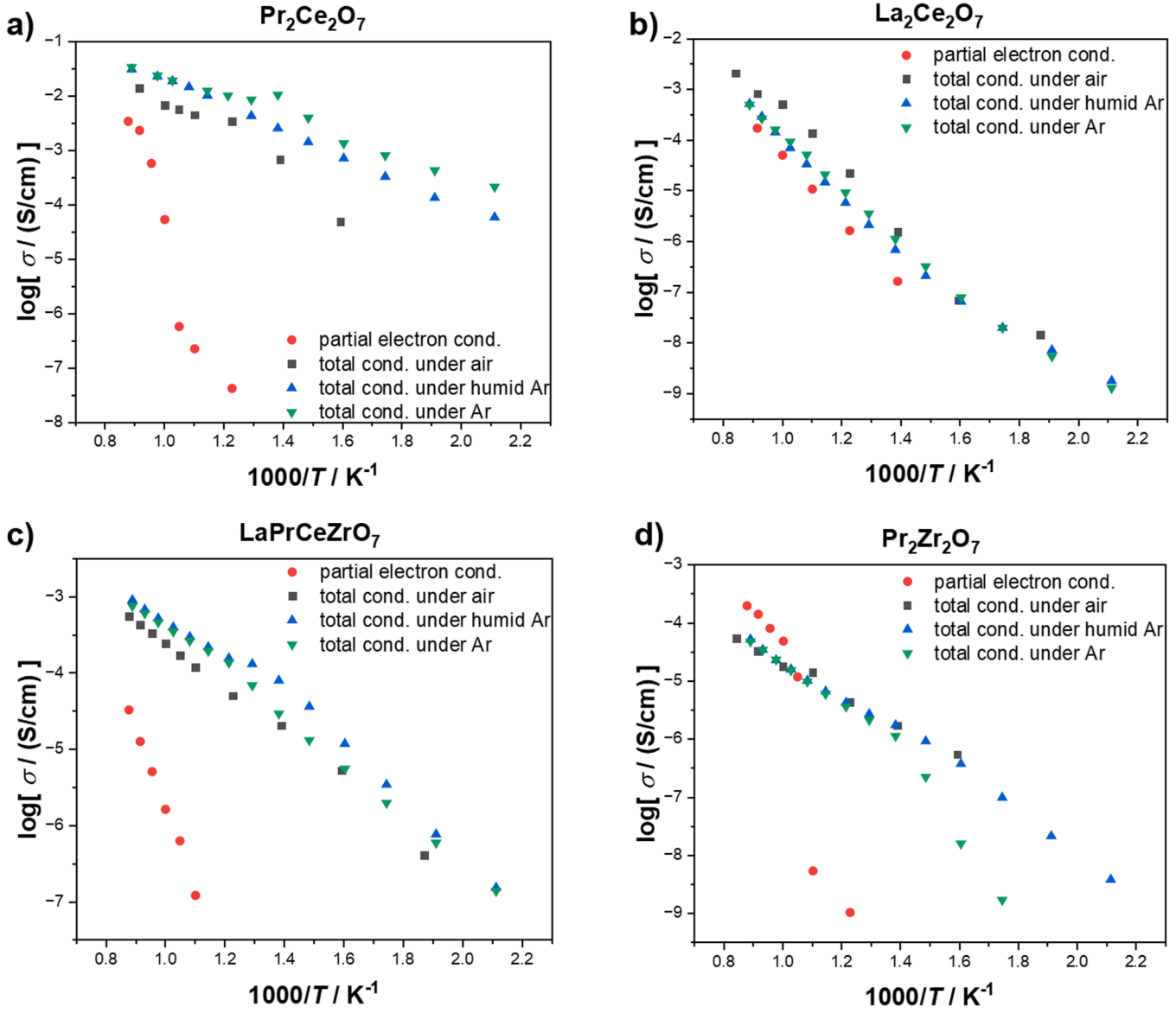

Fig. 5. Impedance spectra of $Pr_2Ce_2O_7$, $La_2Ce_2O_7$, $LaPrCeZrO_7$, and $Pr_2Zr_2O_7$ under air, Ar, and humid Ar alongside the partial electronic conductivity.

around 500 °C, has likewise been reported in the literature and most likely attributed to the reduction of Pr^{4+} to Pr^{3+}. [71,72] As the temperature decreases, the Pr^{4+}/Pr^{3+} equilibrium shifts towards Pr^{3+}, reducing the number of mixed-valence hopping sites available for electronic transport.

The higher total conductivities of $LaPrCeZrO_7$ compared to $Pr_2Zr_2O_7$ may originate from the coexistence of two different redox-active cations, Pr^{3+} and Ce^{4+}. While electronic transport in $Pr_2Zr_2O_7$ primarily relies on Pr^{3+}/Pr^{4+} small-polaron hopping, the additional Ce^{3+}/Ce^{4+} redox couple provides complementary mixed-valence hopping pathways. The presence of both redox couples is expected to increase the connectivity with a more continuous network of redox-active centers for small-polaron transport, reducing dependence on a single hopping mechanism and enhancing electronic transport and total conductivity. Moreover, $LaPrCeZrO_7$ exhibits a higher conductivity under humid Ar than under dry Ar at temperatures below 500 °C, whereas both atmospheres show nearly identical conductivities above 500 °C. As the temperature decreases further, the conductivity curves converge again at around 200 °C, which is in line with a reduced proton mobility at lower temperatures. [73] This behavior suggests that the additional conductivity under humid conditions is limited to the intermediate temperature range (300–500 °C) and is most likely associated with proton conduction.

For $La_2Ce_2O_7$, there are only minor differences between air, Ar, and humid Ar. In our work, demonstrated that under Ar atmosphere (both wet and dry under high temperatures) the conductivity is lower compared to the total conductivity measured under air as fewer oxygen ions are present and the ionic conductivity decreases. Moreover, under an Ar atmosphere oxygen from interstitial sites can escape the structure and lead to Ce^{3+} formation which can enhance electronic conductivity, but does not compensate for the decrease in ionic conductivity of $La_2Ce_2O_7$. The electronic conductivity measured with Hebb-Wagner is still the lowest overall. By comparing the partial electronic conductivity with the total conductivity measured under air, the electronic conductivity is about one order of magnitude lower, which shows that the ionic conductivity is still the main factor in the overall conductivity. Besikiotis et al. also reported an independence of pO_2 of the total conductivity of $La_2Ce_2O_7$, with the conductivity primarily consisting of an ionic contribution. [74] The minor variations observed among the atmospheres reflect small disparities in defect concentrations and redox states, rather than a fundamental shift in the conduction mechanism. At temperatures below 300 °C, the conductivity measured under humid Ar shows a slight increase, indicating that proton conduction may contribute in this temperature range. A similar enhancement of proton conduction was reported for $La_2Ce_2O_7$ with a well-defined fluorite structure, suggesting that a highly ordered crystal structure without additional defects or pyrochlore-related features in the microstructure is favorable for proton transport mechanisms. [75] It has been shown by Sun et al. that the activation energy is generally lower under wet conditions than under dry conditions, decreasing by 0.3 eV from around 1.2 eV to 0.9 eV with achieving $6.68 \bullet 10^{-5}$ and $4.98 \bullet 10^{-7}$ S cm^{-1} in wet air at 550 and 250 °C, respectively. [75] In this work, in wet Ar $5.85 \bullet 10^{-6}$ and $7.27 \bullet 10^{-9}$ S cm^{-1} were measured. The activation energy for $La_2Ce_2O_7$ in dry and wet Ar in the 200 – 400 °C temperature range is lower with 0.64 eV, but does not change from dry to wet conditions. It has to be noted that this study used 50% humidity as wet Ar, whereas the literature often uses only 2–3% H_2O. Moreover, it is possible that a hydration throughout the bulk is hindered by proton conduction pathways being partially blocked by partial pyrochlore-like ordering of the structure.

For $Pr_2Ce_2O_7$, the total conductivity under air is lower than under Ar and humid Ar across the measured temperature range with the highest conductivity measured under Ar with the lowest activation energies with (0.30 ± 0.02) eV at 500 – 850 °C and (0.31 ± 0.01) eV at 200 – 400 °C (Table 1), which is even lower compared to the activation energies measured under wet Ar. The lower total conductivity of $Pr_2Ce_2O_7$ under air compared to Ar and humid Ar can further be assigned to the high oxygen partial pressure, which reduces the concentration of oxygen vacancies and shifts the Ce^{3+}/Ce^{4+} and Pr^{3+}/Pr^{4+} redox equilibrium with mostly Pr^{3+} present, thereby limiting both ionic and electronic transport. Although the nominal stoichiometry corresponds to a Pr^{3+}/Ce^{4+} system, the actual electronic structure is not purely Pr^{3+}-based: the Ce^{4+}-rich environment stabilizes a small but functionally crucial fraction of Pr^{4+}, establishing a Pr^{3+}/Pr^{4+} redox equilibrium in the lattice. This mixed-valence state enables a pronounced contribution from electronic conduction at temperatures below roughly 500 °C, *via* small-polaron hopping between Pr^{3+} and Pr^{4+} sites. [76,77] When the material is exposed to a humid atmosphere, water vapor acts as a reducing agent and shifts the redox equilibrium towards Pr^{3+} by reducing Pr^{4+}. At the same time, H_2O is incorporated into the lattice by forming hydroxyl groups, which bind to intrinsic oxygen vacancies *via* [28]:

$$H_2O + V_O^{\bullet\bullet} + O_O^X \leftrightarrow 2\ OH_O^{\bullet} \quad (5)$$

These two processes—(i) the suppression of electronic conductivity due to depletion of Pr^{4+} sites and (ii) the blocking of oxygen-ion transport by OH- formation—lead to increased resistances below 500 °C in humid conditions compared to dry Ar. Even a small shift in the Pr^{3+}/Pr^{4+} ratio has a disproportionately large impact on the total conductivity. Above approximately 500–600 °C, however, hydroxyl groups become thermally unstable and desorb, and the Pr redox equilibrium is increasingly governed by temperature and the oxygen sublattice rather than by H_2O. [18] As a result, the influence of humidity on the Pr oxidation state becomes negligible, and the conductivity becomes dominated by intrinsic oxygen-ion transport, which is largely insensitive to ambient humidity. Additional contributions may arise from surface adsorption effects and subtle shifts in the local redox balance. [78]

In acceptor-doped zirconates, the partial electronic conductivities derived from Hebb–Wagner measurements may exhibit values that exceed the total conductivity determined through EIS at temperatures above 700 °C. This can be assigned to the potential violation of Hebb–Wagner assumptions under high-temperature direct current (DC) conditions. Zirconates often show low electronic conductivity and a low redox buffering capacity. At high temperatures, an applied DC field can therefore induce local chemical potential gradients and field-driven reduction near the electrodes, leading to a locally enhanced electronic conductivity that is not representative of the bulk which is strongly discussed by in the literature [79–81]. Hebb–Wagner measurements probe this locally perturbed state, whereas EIS continues to measure the volume-averaged, near-equilibrium conductivity. Below 700 °C, defect mobility and electrode reaction kinetics in zirconates are strongly

Table 1
Activation energies of all compounds with their temperature range for partial electronic conductivity, total conductivity measured under air, under Ar, and under humid Ar.

	$E_{A\ (part.\ eletr.)}$ / eV (temp. range / °C)	$E_{A\ (under\ air)}$ / eV (temp. range / °C)	$E_{A\ (under\ Ar)}$ / eV (temp. range / °C)	$E_{A\ (under\ humid\ Ar)}$ / eV (temp. range / °C)
$Pr_2Ce_2O_7$	1.24 ± 0.09 (500 – 650)	1.00 ± 0.07 (300 – 500)	0.31 ± 0.01 (200 – 400)	0.46 ± 0.01 (200 – 500)
	3.82 ± 0.44 (700 – 800)	0.35 ± 0.02 (600 – 750)	0.30 ± 0.02 (500 – 850)	0.37 ± 0.03 (600 – 850)
$La_2Ce_2O_7$	1.27 ± 0.01 (400 – 800)	1.20 ± 0.05 (300 – 850)	0.64 ± 0.01 (200 – 350)	0.64 ± 0.03 (200 – 450)
			1.05 ± 0.01 (350 – 850)	1.16 ± 0.01 (450 – 850)
$LaPrCeZrO_7$	2.10 ± 0.06 (650 – 850)	0.60 ± 0.02 (250 – 850)	0.64 ± 0.01 (200 – 500)	0.75 ± 0.01 (200 – 450)
			0.45 ± 0.01 (550 – 850)	0.46 ± 0.01 (550 – 850)
$Pr_2Zr_2O_7$	0.99 ± 0.05 (700 – 850)	0.53 ± 0.02 (350 – 850)	1.58 ± 0.07 (300 – 450)	0.76 ± 0.01 (200 – 400)
			0.65 ± 0.01 (450 – 850)	0.63 ± 0.02 (500 – 850)

reduced, the material remains chemically homogeneous, and the Hebb–Wagner assumptions are fulfilled again. Further analysis of the ionic transport properties reveals that $Pr_2Zr_2O_7$ demonstrates the most pronounced increase in conductivity under humid Ar conditions, accompanied by the highest proton transference number with $t_{H^+} = \frac{\sigma_{\text{humid Ar}} - \sigma_{\text{Ar}}}{\sigma_{\text{humid Ar}}} \approx 0.98$ at 300 °C in this temperature range among all compounds. This behavior can be attributed to the uptake of water, which enables proton conduction *via* mobile hydroxyl species. [82] The redox-inactive Zr^{4+} cations limit electronic transport, making the protonic contribution more pronounced. Furthermore, the compound exhibits a well-defined pyrochlore structure without any detectable secondary phases, as confirmed by structural characterization, which likely supports efficient proton transport through the structure and along grain boundaries. At temperatures above 500 °C, dehydration occurs, leading to a loss of mobile protons, and the conductivity of both systems is dominated by intrinsic oxygen-ion transport and the conductivities under dry and humid conditions converge. Overall, the results demonstrate how the interplay of structure and cation chemistry governs the transport properties, with proton conduction being particularly pronounced in Zr-containing pyrochlores under humid conditions, facilitated by their stable pyrochlore structure.

4. Conclusions and outlook

Overall, our investigation provides a comprehensive understanding of how structural motifs influence electronic, protonic, and oxygen ion conductivity in compounds evolved from the fluorite phase, ranging from disordered phases to well-defined pyrochlore structures. By analyzing work function, band gap, and partial transport characteristics, we identify clear correlations between specific structural motifs and charge transport properties, underscoring the crucial role of redox-active elements. Hebb–Wagner polarization measurements revealed pronounced composition-, temperature-, and oxygen partial pressure–dependent electronic transport in the investigated pyrochlores. Ce-based compositions exhibit a strong pO_2 dependence of the electronic partial conductivity, which is in good accordance to simulations. Hebb–Wagner measurements of the partial electronic conductivity in ceria-based materials exhibit a $-1/6$ slope near the conductivity minimum. The $-1/4$ regime expected from the Brouwer diagram is strongly compressed or not experimentally accessible, since reduction-induced oxygen vacancies become transport-dominant at comparatively high pO_2. Moreover, the nature of the acceptor-doped A-site cation does not directly cause the occurrence of the $-1/6$ slope, it rather shifts the equilibrium position, with Pr stabilizing it at higher oxygen partial pressures. In contrast, zirconate-based pyrochlores exhibit an electronic conductivity that is nearly independent of oxygen partial pressure, consistent with a more stable defect chemistry. EIS measurements performed under air, Ar, and humidified Ar atmospheres revealed pronounced proton conduction in $Pr_2Zr_2O_7$ at temperatures below 500 °C, with proton transport contributing almost exclusively to the total conductivity. In contrast, $Pr_2Ce_2O_7$ exhibited a decrease in conductivity under humidified Ar which goes back to water uptake at oxygen vacancy sites and effectively blocks conduction pathways and promotes the reduction of Pr^{4+} to Pr^{3+}. As a result, the concentration of oxygen vacancies is reduced, and the Ce^{3+}/Ce^{4+} and Pr^{3+}/Pr^{4+} redox equilibria shift toward predominantly Pr^{3+}, thereby limiting both ionic and electronic transport. Moreover, it was found that compounds with well-defined crystal structures and low disorder show higher conductivity. In particular, the pyrochlore phase, which intrinsically accommodates oxygen vacancies within its ordered structure, showed enhanced transport properties for protons compared to more disordered or defect-rich materials. Taken together, the results offer valuable guidance for the rational design of pyrochlore materials with tailored properties for energy conversion and electronic applications.

CRediT authorship contribution statement

Patrick Mowe: Conceptualization; Data curation; Formal analysis; Investigation; Methodology; Validation; Visualization; Writing – original draft; Writing – review & editing. **Hauke Glück:** Data curation; Writing – review & editing. **Thomas Jüstel:** Writing – review & editing. **Martin Winter:** Supervision; Writing – review & editing. **Kerstin Neuhaus:** Funding acquisition; Project administration; Supervision; Writing – original draft; Writing – review & editing.

Funding

The study is funded by the Deutsche Forschungsgemeinschaft (DFG), project number 523164409.

Declaration of Competing Interest

There are no conflicts to declare.

Acknowledgements

The authors thank Prof. Roger De Souza and Prof. Igor Lubomirsky for help and discussion. Additional thanks go to Dr. David Enseling for help with the reflectance measurements.

Appendix A. Supporting information

Supplementary data associated with this article can be found in the online version at doi:10.1016/j.jallcom.2026.190998.

Data availability

Data will be made available on request.

References

[1] E.D. Wachsman, K.T. Lee, Lowering the temperature of solid oxide fuel cells, Science 334 (2011) 935–939, https://doi.org/10.1126/science.1204090.
[2] Z. Zakaria, S.H. Abu Hassan, N. Shaari, A.Z. Yahaya, Y. Boon Kar, A review on recent status and challenges of yttria stabilized zirconia modification to lowering the temperature of solid oxide fuel cells operation, Int. J. Energy Res. 44 (2020) 631–650, https://doi.org/10.1002/er.4944.
[3] M.N. Sravanthi, J. Sudagar, Structural, optical, and dielectric properties of zirconium titanate ceramic composite synthesized by solid-state reaction, J. Mater. Eng. Perform. 33 (2024) 12133–12143, https://doi.org/10.1007/s11665-023-08827-z.
[4] Q. Zhang, X. Li, J. Shen, G. Wu, J. Wang, L. Chen, ZrO2 thin films and ZrO2/SiO2 optical reflection filters deposited by sol–gel method, Mater. Lett. 45 (2000) 311–314, https://doi.org/10.1016/S0167-577X(00)00124-5.
[5] M. Coduri, S. Checchia, M. Longhi, D. Ceresoli, M. Scavini, Rare earth doped ceria: the complex connection between structure and properties, Front. Chem. 6 (2018) 526, https://doi.org/10.3389/fchem.2018.00526.
[6] Z. Zhu, W. Sun, Z. Wang, J. Cao, Y. Dong, W. Liu, A high stability Ni–La 0.5 Ce 0.5 O 2−δ asymmetrical metal-ceramic membrane for hydrogen separation and generation, J. Power Sources 281 (2015) 417–424, https://doi.org/10.1016/j.jpowsour.2015.02.005.
[7] J. Diazguillen, M. Diazguillen, K. Padmasree, A. Fuentes, J. Santamaria, C. Leon, High ionic conductivity in the pyrochlore-type Gd2−yLayZr2O7 solid solution (0≤y≤1), Solid. State Ion. 179 (2008) 2160–2164, https://doi.org/10.1016/j.ssi.2008.07.015.
[8] N. Mahato, A. Banerjee, A. Gupta, S. Omar, K. Balani, Progress in material selection for solid oxide fuel cell technology: a review, Prog. Mater. Sci. 72 (2015) 141–337, https://doi.org/10.1016/j.pmatsci.2015.01.001.
[9] B. Choudhary, L. Besra, S. Anwar, S. Anwar, La2Ce2O7 based materials for next generation proton conducting solid oxide cells: progress, opportunity and future prospects, Int. J. Hydrog. Energy 48 (2023) 28460–28501, https://doi.org/10.1016/j.ijhydene.2023.03.393.
[10] K.-Z. Fung, S.-Y. Tsai, Evaluation of La2Ce2O7 (LCO) protection layer for proton conducting electrolyte, ECS Meet. Abstr. MA2022-02 (2022), https://doi.org/10.1149/MA2022-02471787mtgabs.
[11] B. Choudhary, S. Anwar, Fabrication of fuel electrode supported proton conducting SOFC via EPD of La2Ce2O7 electrolyte and its performance evaluation, Solid State Ion. 401 (2023) 116356, https://doi.org/10.1016/j.ssi.2023.116356.
[12] E. Aneggi, M. Boaro, C.D. Leitenburg, G. Dolcetti, A. Trovarelli, Insights into the redox properties of ceria-based oxides and their implications in catalysis, J. Alloy.

Compd. 408–412 (2006) 1096–1102, https://doi.org/10.1016/j.jallcom.2004.12.113.
[13] B. Matović, J. Maletaškić, K. Yoshida, T. Yano, Synthesis, characterization and sintering of fluorite and pyrochlore-type compounds: Pr2Zr2O7, Sm2Zr2O7 and PrSmZr2O7, Mater. Today Proc. 16 (2019) 156–162, https://doi.org/10.1016/j.matpr.2019.05.283.
[14] H.L. Tuller, S.R. Bishop, D. Chen, Y. Kuru, J.-J. Kim, T.S. Stefanik, Praseodymium doped ceria: Model mixed ionic electronic conductor with coupled electrical, optical, mechanical and chemical properties, Solid. State Ion. 225 (2012) 194–197, https://doi.org/10.1016/j.ssi.2012.02.029.
[15] S. Fahed, R. Pointecouteau, M. Aouine, A. Boréave, S. Gil, V. Meille, P. Bazin, O. Toulemonde, A. Demourgues, M. Daturi, P. Vernoux, Pr-rich cerium-zirconium-praseodymium mixed oxides for automotive exhaust emission control, Appl. Catal. Gen. 644 (2022) 118800, https://doi.org/10.1016/j.apcata.2022.118800.
[16] J.A. Kilner, Defects and Conductivity in Ceria-based Oxides, Chem. Lett. 37 (2008) 1012–1015, https://doi.org/10.1246/cl.2008.1012.
[17] J. Abel, M. Lamirand-Majimel, J. Majimel, V. Bellière-Baca, V. Harlé, G. André, C. Prestipino, S. Figueroa, E. Durand, A. Demourgues, Oxygen non-stoichiometry phenomena in $Pr_{1-x}Zr_xO_{2-y}$ compounds ($0.02 < x < 0.5$), Dalton Trans. 43 (2014) 15183–15191, https://doi.org/10.1039/C4DT01545B.
[18] A.V. Shlyakhtina, J.C.C. Abrantes, E. Gomes, A.N. Shchegolikhin, G.A. Vorobieva, K.I. Maslakov, A.V. Knotko, L.G. Shcherbakova, Effect of Pr3+/Pr4+ ratio on the oxygen ion transport and thermomechanical properties of the pyrochlore and fluorite phases in the ZrO2–Pr2O3 system, Int. J. Hydrog. Energy 41 (2016) 9982–9992, https://doi.org/10.1016/j.ijhydene.2016.02.152.
[19] D.A. Belov, A.V. Shlyakhtina, J.C.C. Abrantes, S.A. Chernyak, G.A. Gasymova, O. K. Karyagina, L.G. Shcherbakova, Electrochemical behavior of the pyrochlore- and fluorite-like solid solutions in the Pr2O3–ZrO2 system. Part I, Solid. State Ion. 271 (2015) 79–85, https://doi.org/10.1016/j.ssi.2014.09.035.
[20] B.P. Mandal, A.K. Tyagi, Ionic conductivity in materials with a pyrochlore structure. Pyrochlore Ceram, Elsevier, 2022, pp. 277–294, https://doi.org/10.1016/B978-0-323-90483-4.00007-6.
[21] M. Pokhrel, S.K. Gupta, K. Wahid, Y. Mao, Pyrochlore Rare-Earth Hafnate $RE_2Hf_2O_7$ (RE = La and Pr) Nanoparticles Stabilized by Molten-Salt Synthesis at Low Temperature, Inorg. Chem. 58 (2019) 1241–1251, https://doi.org/10.1021/acs.inorgchem.8b02728.
[22] P.Pechini Maggio, n.d. Method of preparing lead and alkaline earth titanates and niobates and coating method using the same to form a capacitor, SPRAGUE ELECTRIC CO, US, 1967, pp. 30–50.
[23] E. Reynolds, P.E.R. Blanchard, Q. Zhou, B.J. Kennedy, Z. Zhang, L.-Y. Jang, Structural and spectroscopic studies of La 2 Ce 2 O 7: Disordered fluorite versus pyrochlore structure, Phys. Rev. B 85 (2012) 132101, https://doi.org/10.1103/PhysRevB.85.132101.
[24] D.E.P. Vanpoucke, P. Bultinck, S. Cottenier, V. Van Speybroeck, I. Van Driessche, Density functional theory study of La 2 Ce 2 O 7: Disordered fluorite versus pyrochlore structure, Phys. Rev. B 84 (2011) 054110, https://doi.org/10.1103/PhysRevB.84.054110.
[25] C. Wang, Y. Wang, A. Zhang, Y. Cheng, F. Chi, Z. Yu, The influence of ionic radii on the grain growth and sintering-resistance of Ln2Ce2O7 (Ln = La, Nd, Sm, Gd), J. Mater. Sci. 48 (2013) 8133–8139, https://doi.org/10.1007/s10853-013-7625-x.
[26] J. Zamudio-García, L.D. Santos-Gómez, J.M. Porras-Vázquez, E.R. Losilla, D. Marrero-López, Doping effects on the structure and electrical properties of La2Ce2O7 proton conductors, J. Alloy. Compd. 816 (2020) 152600, https://doi.org/10.1016/j.jallcom.2019.152600.
[27] Q. Zhang, X. Zheng, J. Jiang, W. Liu, Structural Stability of $La_2Ce_2O_7$ as a Proton Conductor: A First-Principles Study, J. Phys. Chem. C. 117 (2013) 20379–20386, https://doi.org/10.1021/jp403660y.
[28] P. Mowe, F. Pfeiffer, O. Maus, W.G. Zeier, M. Winter, K. Neuhaus, Relationship between structure and room-temperature charge transport in highly acceptor-doped ceria and zirconia, Solid. State Ion. 428 (2025) 116955, https://doi.org/10.1016/j.ssi.2025.116955.
[29] F. Zhong, S. Yang, C. Chen, H. Fang, K. Chen, C. Zhou, L. Lin, Y. Luo, C. Au, L. Jiang, Defect-induced pyrochlore Pr2Zr2O7 cathode rich in oxygen vacancies for direct ammonia solid oxide fuel cells, J. Power Sources 520 (2022) 230847, https://doi.org/10.1016/j.jpowsour.2021.230847.
[30] S. Mahapatra, S.S. Behera, R. Rawat, S. Singh, Crystal growth of pyrochlore Pr 2 Zr 2 O 7 and its La and Nd analogs using flux method, J. Cryst. Growth 667 (2025) 128234, https://doi.org/10.1016/j.jcrysgro.2025.128234.
[31] A. Panghal, Y. Kumar, P.K. Kulriya, P.M. Shirage, N.L. Singh, Structural assessment and irradiation response of La2Zr2O7 pyrochlore: Impact of irradiation temperature and ion fluence, J. Alloy. Compd. 862 (2021) 158556, https://doi.org/10.1016/j.jallcom.2020.158556.
[32] M.T. Vandenborre, E. Husson, Comparison of the force field in various pyrochlore families. I. The A2B2O7 oxides, J. Solid. State Chem. 50 (1983) 362–371, https://doi.org/10.1016/0022-4596(83)90205-0.
[33] F.X. Zhang, C.L. Tracy, M. Lang, R.C. Ewing, Stability of fluorite-type La2Ce2O7 under extreme conditions, J. Alloy. Compd. 674 (2016) 168–173, https://doi.org/10.1016/j.jallcom.2016.03.002.
[34] J.R. McBride, K.C. Hass, B.D. Poindexter, W.H. Weber, Raman and x-ray studies of $Ce1-xRExO2-y$, where RE=La, Pr, Nd, Eu, Gd, and Tb, J. Appl. Phys. 76 (1994) 2435–2441, https://doi.org/10.1063/1.357593.
[35] J. Xu, Y. Zhang, Y. Liu, X. Fang, X. Xu, W. Liu, R. Zheng, X. Wang, Optimizing the Reaction Performance of $La_2Ce_2O_7$ -Based Catalysts for Oxidative Coupling of Methane (OCM) at Lower Temperature by Lattice Doping with Ca Cations, Eur. J. Inorg. Chem. 2019 (2019) 183–194, https://doi.org/10.1002/ejic.201801250.
[36] B. Choudhary, S. Anwar, D.A. Medvedev, L. Besra, S. Anwar, Effect of sintering temperature on the transport properties of La2Ce2O7 ceramic materials, Ceram. Int. 48 (2022) 6758–6766, https://doi.org/10.1016/j.ceramint.2021.11.227.
[37] M.L. Sanjuán, R.I. Merino, A.K. Lakshya, A. Chowdhury, Spectroscopic insight into the structural and microstructural properties of La2Ce2O7 ceramics, Bol. Soc. Esp. Cerámica Vidr. (2024) S0366317524000220, https://doi.org/10.1016/j.bsecv.2024.07.002.
[38] W. Melitz, J. Shen, A.C. Kummel, S. Lee, Kelvin probe force microscopy and its application, Surf. Sci. Rep. 66 (2011) 1–27, https://doi.org/10.1016/j.surfrep.2010.10.001.
[39] N. Ishida, Influence of Fermi level pinning on contact potential difference measurements using Kelvin probe force microscopy, Phys. Rev. B 111 (2025) 125304, https://doi.org/10.1103/PhysRevB.111.125304.
[40] M. Da Lisca, J. Alvarez, J.P. Connolly, N. Vaissiere, K. Mekhazni, J. Decobert, J.-P. Kleider, Cross-sectional Kelvin probe force microscopy on III–V epitaxial multilayer stacks: challenges and perspectives, Beilstein J. Nanotechnol. 14 (2023) 725–737, https://doi.org/10.3762/bjnano.14.59.
[41] A. Klein, C. Körber, A. Wachau, F. Säuberlich, Y. Gassenbauer, S.P. Harvey, D. E. Proffit, T.O. Mason, Transparent Conducting Oxides for Photovoltaics: Manipulation of Fermi Level, Work Function and Energy Band Alignment, Materials 3 (2010) 4892–4914, https://doi.org/10.3390/ma3114892.
[42] S. Zinatloo-Ajabshir, E. Shafaati, A. Bahrami, Facile fabrication of efficient Pr2Ce2O7 ceramic nanostructure for enhanced photocatalytic performances under solar light, Ceram. Int. 48 (2022) 24695–24705, https://doi.org/10.1016/j.ceramint.2022.05.116.
[43] S.A. Heidari-Asil, S. Zinatloo-Ajabshir, O. Amiri, M. Salavati-Niasari, Amino acid assisted-synthesis and characterization of magnetically retrievable ZnCo2O4–Co3O4 nanostructures as high activity visible-light-driven photocatalyst, Int. J. Hydrog. Energy 45 (2020) 22761–22774, https://doi.org/10.1016/j.ijhydene.2020.06.122.
[44] P. Makuła, M. Pacia, W. Macyk, How To Correctly Determine the Band Gap Energy of Modified Semiconductor Photocatalysts Based on UV–Vis Spectra, J. Phys. Chem. Lett. 9 (2018) 6814–6817, https://doi.org/10.1021/acs.jpclett.8b02892.
[45] S. Zinatloo-Ajabshir, Z. Salehi, O. Amiri, M. Salavati-Niasari, Simple fabrication of Pr2Ce2O7 nanostructures via a new and eco-friendly route; a potential electrochemical hydrogen storage material, J. Alloy. Compd. 791 (2019) 792–799, https://doi.org/10.1016/j.jallcom.2019.04.005.
[46] A.A. Ansari, S.P. Singh, B.D. Malhotra, Optical and structural properties of nanostructured CeO2:Tb3+ film, J. Alloy. Compd. 509 (2011) 262–265, https://doi.org/10.1016/j.jallcom.2010.07.009.
[47] S. Khademinia, M. Behzad, Lanthanum cerate (La2Ce2O7): hydrothermal synthesis, characterization and optical properties, Int. Nano Lett. 5 (2015) 101–107, https://doi.org/10.1007/s40089-015-0143-x.
[48] Y. Xu, H. Man, N. Tang, T. Ohtsuki, S. Baidya, S. Nakatsuji, D. Vanderbilt, N. Drichko, Phonon spectrum of Pr 2 Zr 2 O 7 and Pr 2 Ir 2 O 7 as evidence of coupling of the lattice with electronic and magnetic degrees of freedom, Phys. Rev. B 105 (2022) 075137, https://doi.org/10.1103/PhysRevB.105.075137.
[49] S. Krämer, J. Hopster, A. Windmüller, R.-A. Eichel, M. Grünebaum, T. Jüstel, M. Winter, K. Neuhaus, Teaching an old dog new tricks: Ti-doped $ZnFe_2O_4$ as active material in zinc ion batteries – a proof of concept, Energy Adv. 3 (2024) 2175–2185, https://doi.org/10.1039/D4YA00134F.
[50] J. Ouyang, Y. Peng, W. Zhou, X. Liang, G. Wang, Q. Zhang, B. Yuan, The Role of Oxygen Vacancies in Phase Transition and the Optical Absorption Properties within Nanocrystalline ZrO2, Nanomaterials 14 (2024) 967, https://doi.org/10.3390/nano14110967.
[51] N. Fifere, A. Airinei, M. Dobromir, L. Sacarescu, S.I. Dunca, Revealing the effect of synthesis conditions on the structural, optical, and antibacterial properties of cerium oxide nanoparticles, Nanomaterials 11 (2021) 2596, https://doi.org/10.3390/nano11102596.
[52] M.H. Hebb, Electrical conductivity of silver sulfide, J. Chem. Phys. 20 (1952) 185–190, https://doi.org/10.1063/1.1700165.
[53] C. Wagner, Galvanische Zellen mit festen Elektrolyten mit gemischter Stromleitung, Z. Für Elektrochem. Berichte Bunsenges, F. üR. Phys. Chem. 60 (1956) 4–7, https://doi.org/10.1002/bbpc.19560600104.
[54] S. Cheng, C. Chatzichristodoulou, M. Søgaard, A. Kaiser, P.V. Hendriksen, Ionic/Electronic Conductivity, Thermal/Chemical Expansion and Oxygen Permeation in Pr and Gd Co-Doped Ceria $Pr_xGd_{0.1}Ce_{0.9-x}O_{1.95-\delta}$, J. Electrochem. Soc. 164 (2017) F1354–F1367, https://doi.org/10.1149/2.0531713jes.
[55] S.R. Bishop, T.S. Stefanik, H.L. Tuller, Defects and transport in $Pr_xCe_{1-x}O_{2-\delta}$: Composition trends, J. Mater. Res. 27 (2012) 2009–2016, https://doi.org/10.1557/jmr.2012.130.
[56] S. Lübke, H.-D. Wiemhöfer, Electronic conductivity of Gd-doped ceria with additional Pr-doping, Solid. State Ion. 117 (1999) 229–243, https://doi.org/10.1016/S0167-2738(98)00408-1.
[57] S. Zhang, J. Xu, C. Lu, R. Ouyang, J. Ma, X. Zhong, X. Fang, X. Xu, X. Wang, Preparation method investigation and structure identification by XRD and Raman techniques for $A_2B_2O_7$ composite oxides, J. Am. Ceram. Soc. 107 (2024) 3475–3496, https://doi.org/10.1111/jace.19645.
[58] K. Neuhaus, Jupyter Notebook for Interactive Brouwer Diagram Simulation of Acceptor-Doped Cerium Dioxide, (2026). https://doi.org/10.5281/ZENODO.19369689.
[59] J.-P. Eufinger, M. Daniels, K. Schmale, S. Berendts, G. Ulbrich, M. Lerch, H.-D. Wiemhöfer, J. Janek, The model case of an oxygen storage catalyst – non-stoichiometry, point defects and electrical conductivity of single crystalline CeO_2 –ZrO_2 –Y_2O_3 solid solutions, Phys. Chem. Chem. Phys. 16 (2014) 25583–25600, https://doi.org/10.1039/C4CP03704A.

[60] S. Grieshammer, R.A. De Souza, Fundamentals of electrical conduction in ceramics, Adv. Ceram. Energy Convers. Storage (2020) 277–320, https://doi.org/10.1016/B978-0-08-102726-4.00007-7.
[61] K. Wang, C. Zhao, N. Wei, J. Yun, X. Hu, X. Jiang, R. Chu, Z. Tong, Y. Zou, Z. Chen, insight into low-temperature styrene oxidation over nano CeO_2 catalysts: modulating Ce–O bond strength to construct oxygen defect engineering, ACS EST Eng. 3 (2023) 1098–1111, https://doi.org/10.1021/acsestengg.2c00376.
[62] S. Tian, J. Cao, Y. Hu, J. Ye, X. Yao, Weakening of CeO bond strength in CeO2 via microwave irradiation treatment to boost toluene catalytic oxidation over NiMnOx/CeO2 catalysts: Performance and reaction mechanism, Sep. Purif. Technol. 397 (2026) 138097, https://doi.org/10.1016/j.seppur.2026.138097.
[63] L. Schweiger, K. Hogrefe, B. Gadermaier, J.L.M. Rupp, H.M.R. Wilkening, Ionic conductivity of nanocrystalline and amorphous Li_{10} GeP_2 S_{12}: the detrimental impact of local disorder on ion transport, J. Am. Chem. Soc. 144 (2022) 9597–9609, https://doi.org/10.1021/jacs.1c13477.
[64] Z.-G. Liu, J.-H. Ouyang, Y. Zhou, X.-L. Xia, Electrical conductivity and thermal expansion of neodymium–ytterbium zirconate ceramics, J. Power Sources 195 (2010) 3261–3265, https://doi.org/10.1016/j.jpowsour.2009.11.135.
[65] E. Celik, A. Usler, M. Wiche, A. Mazilkin, T. Brezesinski, R.A. De Souza, M.T. Elm, Unexpectedly high electronic partial conductivity of porous yttria-stabilized zirconia thin films, J. Phys. Chem. C. 129 (2025) 12585–12594, https://doi.org/10.1021/acs.jpcc.5c02744.
[66] V. Frizon, J.-M. Bassat, M. Pollet, E. Durand, J. Hernandez, K. Pajot, P. Vernoux, A. Demourgues, Tuning the Pr valence state to design high oxygen mobility, redox and transport properties in the CeO_2 –ZrO_2 –PrO $_x$ Phase Diagram, J. Phys. Chem. C. 123 (2019) 6351–6362, https://doi.org/10.1021/acs.jpcc.8b11469.
[67] E.L. Dos Santos Veiga, X.V. Villafruela, J. Llorca, H. Beltrán-Mir, E. Cordoncillo, The catalytic activity of the Pr_2 Zr_{2-x} Fe $_x$ $O_{7\pm\delta}$ system for the CO oxidation reaction, J. Am. Ceram. Soc. 106 (2023) 1369–1380, https://doi.org/10.1111/jace.18846.
[68] A.F. Fuentes, E.C. O'Quinn, S.M. Montemayor, H. Zhou, M. Lang, R.C. Ewing, Pyrochlore-type lanthanide titanates and zirconates: synthesis, structural peculiarities, and properties, Appl. Phys. Rev. 11 (2024) 021337, https://doi.org/10.1063/5.0192415.
[69] K.D. Kreuer, St Adams, W. Münch, A. Fuchs, U. Klock, J. Maier, Proton conducting alkaline earth zirconates and titanates for high drain electrochemical applications, Solid. State Ion. 145 (2001) 295–306, https://doi.org/10.1016/S0167-2738(01)00953-5.
[70] J. Jamnik, J. Maier, Generalised equivalent circuits for mass and charge transport: chemical capacitance and its implications, Phys. Chem. Chem. Phys. 3 (2001) 1668–1678, https://doi.org/10.1039/b100180i.
[71] E.L.D.S. Veiga, M. Fortuño-Morte, H. Beltrán-Mir, E. Cordoncillo, Effect of the oxidation states on the electrical properties of Fe-doped Pr2Zr2O7 pyrochlore, J. Mater. Res. Technol. 16 (2022) 201–215, https://doi.org/10.1016/j.jmrt.2021.11.146.
[72] K. Vasundhara, S.N. Achary, A.K. Tyagi, Structure, thermal and electrical properties of calcium doped pyrochlore type praseodymium zirconate, Int. J. Hydrog. Energy 40 (2015) 4252–4262, https://doi.org/10.1016/j.ijhydene.2015.01.148.
[73] Y. Meng, J. Gao, Z. Zhao, J. Amoroso, J. Tong, K.S. Brinkman, Review: recent progress in low-temperature proton-conducting ceramics, J. Mater. Sci. 54 (2019) 9291–9312, https://doi.org/10.1007/s10853-019-03559-9.
[74] V. Besikiotis, C.S. Knee, I. Ahmed, R. Haugsrud, T. Norby, Crystal structure, hydration and ionic conductivity of the inherently oxygen-deficient La2Ce2O7, Solid. State Ion. 228 (2012) 1–7, https://doi.org/10.1016/j.ssi.2012.08.023.
[75] W. Sun, S. Fang, L. Yan, W. Liu, Investigation on proton conductivity of La_2 Ce_2 O_7 in wet atmosphere: dependence on water vapor partial pressure, Fuel Cells 12 (2012) 457–463, https://doi.org/10.1002/fuce.201100175.
[76] H.L. Tuller, A.S. Nowick, Small polaron electron transport in reduced CeO2 single crystals, J. Phys. Chem. Solids 38 (1977) 859–867, https://doi.org/10.1016/0022-3697(77)90124-X.
[77] C. Chatzichristodoulou, P.V. Hendriksen, Oxygen nonstoichiometry and defect chemistry modeling of Ce[sub 0.8]Pr[sub 0.2]O[sub 2−δ], J. Electrochem. Soc. 157 (2010) B481, https://doi.org/10.1149/1.3288241.
[78] N.S. Leel, M. Kiran, P.A. Alvi, B. Dalela, S. Kumar, S. Dalela, Oxygen vacancies mediated changes in ferromagnetic, optical, Photoluminescent and electronic structure properties of Ho-doped CeO2 nanoparticles, Ceram. Int. 50 (2024) 8448–8462, https://doi.org/10.1016/j.ceramint.2023.12.180.
[79] K.-C. Lee, H.-I. Yoo, Hebb–Wagner-type polarization/relaxation in the presence of the cross effect between electronic and ionic flows in a mixed conductor, J. Phys. Chem. Solids 60 (1999) 911–927, https://doi.org/10.1016/S0022-3697(99)00002-5.
[80] H.-I. Yoo, K.-C. Lee, Failure of the Nernst-Einstein equation and the cross effect between electronic and ionic flows in semiconducting $Co_{1-\delta}$ O, Z. F. üR. Phys. Chem. 207 (1998) 127–146, https://doi.org/10.1524/zpch.1998.207.Part_1_2.127.
[81] H. Yoo, J. Lee, M. Martin, J. Janek, H. Schmalzried, Experimental evidence of the interference between ionic and electronic flows in an oxide with prevailing electronic conduction, Solid. State Ion. 67 (1994) 317–322, https://doi.org/10.1016/0167-2738(94)90024-8.
[82] G. Gregori, M. Shirpour, J. Maier, Proton conduction in dense and porous nanocrystalline ceria thin films, Adv. Funct. Mater. 23 (2013) 5861–5867, https://doi.org/10.1002/adfm.201300527.